# Numerical and experimental investigations on the vibration behavior of a high-speed planetary gearbox

D. Schweigert[1] · B. Morhard[1] · F. Oberneder[1] · L. Pointner-Gabriel[1] · M. Otto[1] · K. Stahl[1]

## Abstract

Increasing the speed of the electric motor can significantly improve the power density of the powertrain of EVs (Electric Vehicles), resulting in a smaller size and thus weight and cost advantages. Achieving acceptable NVH behavior becomes more difficult at higher speeds, partly because the excitation frequencies of the gears cover a wider frequency range and therefore higher natural frequencies can also be directly excited. In the Speed4E joint research project, a high-speed electromechanical powertrain was developed, manufactured, and tested to investigate the main challenges on the NVH- and efficiency-behavior of high-speed powertrains. The high-speed design of the Speed4E drivetrain results in maximum electric motor speeds of up to 50,000 rpm, combined with a torque of up to 45 Nm at the transmission input shafts. This study presents the experimental results on the vibration behavior of the high-speed planetary gearbox, a comparison with the corresponding results of a highly efficient calculation method of the gearbox vibration excitation, and the theoretical background of the calculation method is presented. The results indicate the potential to improve the vibration behavior of high-speed drives in EVs and provide a deep understanding of the challenges associated with high speeds.

## Numerische und experimentelle Untersuchungen zum Schwingungsverhalten eines Hochdrehzahl-Planetengetriebes

### Zusammenfassung

Eine Erhöhung der Drehzahl des Elektromotors kann die Leistungsdichte des Antriebsstrangs von Elektrofahrzeugen erheblich erhöhen, was zu einer kompakteren Bauweise und damit zu Kostenvorteilen führt. Das Erreichen eines akzeptablen NVH-Verhaltens wird mit höheren Drehzahlen schwieriger, insbesondere für das hoch übersetzende Getriebe, das notwendig ist, um ein effizientes Package zu ermöglichen.

Dies wurde im Rahmen des Forschungsprojekts Speed4E untersucht, in dem ein elektromechanischer Hochdrehzahl-Antriebsstrang entwickelt, hergestellt und getestet wurde. Das Design des Speed4E-Antriebsstrangs besitzt maximale Elektromotordrehzahlen von bis zu 50.000 1/min, kombiniert mit einem Drehmoment von bis zu 45 Nm an den Getriebeeingangswellen. In diesem Beitrag werden die experimentellen Ergebnisse zum Schwingungsverhalten des Hochdrehzahl-Planetengetriebes, ein Vergleich mit den entsprechenden Ergebnissen einer hocheffizienten Berechnungsmethode der Getriebe-Schwingungsanregung sowie die theoretischen Grundlagen der Methode vorgestellt. Die Ergebnisse zeigen Potenziale zur Verbesserung des Schwingungsverhaltens von Hochdrehzahlantrieben in BEVs auf und vermitteln ein tiefes Verständnis für die mit sehr hohen Drehzahlen verbundenen Herausforderungen.

✉ D. Schweigert
daniel.schweigert@tum.de

[1] School of Engineering and Design, Department of Mechanical Engineering, Gear Research Center (FZG), Technical University of Munich, Boltzmannstraße 15, 85748 Garching near Munich, Germany

## 1 State of the art

### 1.1 Research project Speed4E

In the Speed4E joint research project [1, 2], a high-speed powertrain for electric vehicles was developed, designed, and investigated. The goals of Speed4E include the development of an innovative powertrain for BEVs with rota-

tional speeds of the electric machines of up to 50,000 rpm, the integration into a test vehicle, and a holistic thermal management based on a water-containing gear fluid. The water-containing gear fluid is used for cooling the power electronics and the electric motors and for lubrication of the gearbox in one circuit. Besides different aspects, the main goal was to optimize efficiency by increasing the power density of the whole system. This can be achieved by increasing the driving speed of the electric machine, since this decreases the torque of the electric machine for the same power level. For Speed4E, the maximum rotational speed of the electric machines was designed to 50,000 rpm on the test rig and to 30,000 rpm on the test vehicle powertrain. Extensive tests of the efficiency and vibration behavior of the powertrain were carried out on the test rigs.

## 1.2 Design of the Speed4E-powertrain

Figure 1 shows a rendering of the Speed4E powertrain with its main components. The high voltage battery, which is not shown, supplies the power electronics with electrical power at a voltage of 800V. The powertrain has an architecture with two electrical machines combined with a high-speed gearbox with a total of three speeds.

The power electronics are contained in a common housing and comprise purpose-built silicon carbide (SiC) modules, capable of switching frequencies of up to 42 kHz. Two different types of electrical machines are used for research purposes. The individual characteristics of each machine can thus be exploited. Sub-transmission 1 (ST1) is driven by an induction machine (IM, EM1) with a max power of 95 kW and max. torque of 60 Nm, whilst sub-transmission 2 (ST2) is driven by a permanent magnet synchronous machine (PMSM, EM2) with a max. power of 135 kW and max. torque of 43 Nm. EM2 is able to rotate to a max. speed of 50,000 rpm, while EM1 has a max. speed of 30,000 rpm. Figure 2 shows the schematic structure (left) and a rendering of the high-speed gearbox with ST1 and ST2 and the differential. ST1 has a fixed gear ratio and contains a plan-
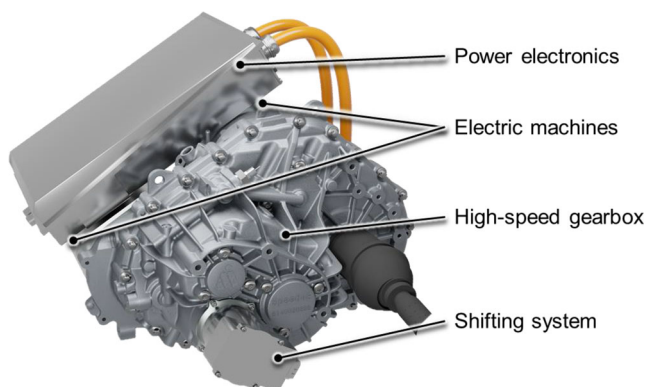


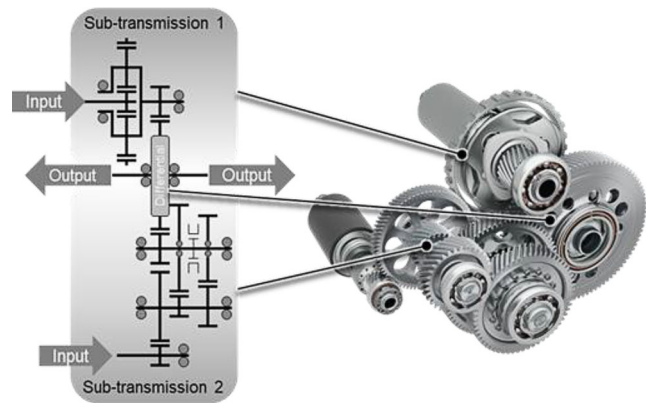**Fig. 1** Speed4E powertrain and its main components



**Fig. 2** Visualization of the high-speed gearbox (right) and its schematic structure (left)

etary gear stage with a gear ratio of 7.25 and a following helical gear stage, which results in an overall gear ratio of 27.5. ST1 is characterized by a high power density and a compact design with a high-ratio planetary gear stage. The shiftable ST2 has two speeds and consists of three helical gear stages. To ensure high torque at low speeds, the first speed shows an overall gear ratio of 36.2. The second speed is designed as an overdrive with a gear ratio of 20.4, which enables the operation of the powertrain in an efficient range of the PMSM at high vehicle speeds. For combining the two independent power paths, both sub-transmissions mesh with the external gearing of the planetary differential [1–3].

## 1.3 High-speed powertrains and calculation of gearbox dynamics

In recent years, a continuing trend towards increasing the maximum drive speeds of electric machines for BEVs can be observed. While the maximum speeds in the early 2010s, as in the case of the BMW i3 vehicle [4], were in the range of just over 10,000 rpm, the most modern electric vehicles like the Tesla Model S plaid already reach maximum speeds over 20,000 rpm. One reason for the increasing maximum speeds is the ability of increasing the power density of the powertrain while maintaining the same mechanical power by using faster turning electric machines [5, 6].

In electric vehicles, the requirements for the vibration behavior of the gearboxes are already more stringent due to the elimination of acoustic masking through the internal combustion engine (ICE) [7, 8]. The challenges regarding gearbox acoustics are further compounded by the increased speeds of the driving machines as the level of excitation increases and a wider frequency range is affected by the tooth frequencies of the meshes or electric machines [9]. For this reason, the vibration behavior of electromechanical

powertrains is the subject of a large number of experimental and numerical investigations.

Chavan et al. [10] investigate the NVH behavior of an e-axis with KissSoft software using an finite element (FE)-based gearbox model, whose large number of degrees of freedom are decoupled by means of modal transformation. The drive system has maximum speeds of up to 13,000 rpm and a coaxial arrangement with a stepped planetary gear. The excitation by the first stage of the planetary gear turns out to be the determining excitation mechanism in the simulation results.

Feng and Qu [11] analyze a drive system with a two-speed spur gearbox using the ROMAX Nexus software, and compare the numerical results with experimental investigations on the e-axis. The electric machine has a maximum speed of 18,000 rpm. This highlights the importance of an early stage identification of NVH related issues, as NVH can be greatly improved by modifying the structure in early stages.

Similar investigations are undertaken by Xianghuan et al. [12] using the simulation software MASTA. Analogous to ROMAX and KissSoft, this is a model on the analytical basis with the inclusion of FE structures. With the help of the simulation tool, the vibration behavior is optimized by adjusting the macro- and micro geometry, which results in a significant improvement of the excitation behavior in simulations and experiments.

Zhang et al. [13] investigate the resonance behavior of a two-stage high-speed helical gearbox using an analytical dynamic computational model. The results show that natural frequencies of the gear stages are of great importance due to the wide range of excitation frequencies in high-speed gearboxes. The gear system is operated at speeds of up to 18,000 rpm even in the supercritical state.

Mbarek et al. [14] use the frequency response method to describe the dynamic behavior of a planetary gearbox, and compare the determined natural frequencies with experimentally determined natural modes. This procedure shows good agreement in the prediction of characteristic natural frequencies.

Inalpolat and Kahraman in [15] investigate the characteristics of sidebands in planetary gears with different numbers of planets and meshing sequences experimentally and numerically. They show that in the case of a symmetric meshing sequence, the tooth meshing order per se has the highest amplitudes and sidebands spaced by integer carrier orders are approximately symmetric about it. In contrast, the tooth meshing order is suppressed in the case of a sequential meshing sequence, whereby the maximum amplitudes occur at a distance of integer carrier orders and in an asymmetrical shape.

The aforementioned studies, as well as a large number of other studies on the NVH behavior of gearboxes in e-mo-

bility, particularly identify resonance phenomena between structural elements and the gear meshing frequencies as the determining factors. For the practical suitability of high-speed gearboxes in electromechanical powertrains, knowledge, as well as mitigation of resonance phenomena, are therefore of utmost importance.

## 1.4 Frequency response procedure for efficient quasi-dynamic simulation of the vibration behavior

In this section, a frequency response method is presented to simulate the quasi-dynamic vibration behavior of the high-speed planetary gearbox in ST1. The method is based on the perturbation calculation approach following the procedure of Kücükay and Bihr [16, 17], who, neglecting the time-varying damping, use the general system of differential equations of motion of an elastic shaft-bearing system and the time average as a starting point:

$$M \cdot \ddot{x} + K_0 \cdot \dot{x} + (C_0 + \varepsilon C_d(t)) \cdot x = f_0 + \varepsilon f_d(t) \quad (1)$$

$M$    Mass matrix (kg)
$x$    Position vector (m)
$K_0$    Constant average damping matrix
$C_0$    Constant, average stiffness matrix (N/s²)
$\varepsilon$    Denotes the smallness of the time-variable components
$C_d$    Time-varying stiffness matrix (N/m)
$f_0$    Constant average load vector (N; Nm)
$f_d$    Time-varying load vector (N; Nm)

The smallness of the time-variable components is characterized by the prefactor $\varepsilon$. The solution according to the approach of the perturbation calculation is further limited to:

$$\varepsilon^0 : M \cdot \ddot{x}_0 + K_0 \cdot \dot{x}_0 + C_0 \cdot x_0 = f_0 \quad (2)$$

and

$$\varepsilon^1 : M \cdot \ddot{x}_1 + K_0 \cdot \dot{x}_1 + C_0 \cdot x_1 = -C_d(t) \cdot x_0 + f_d(t) \quad (3)$$

The static solution of the system ($\varepsilon^0$) can be calculated following (2), formula (3) is an externally excited linear differential equation system representing the dynamic behavior ($\varepsilon^1$) of the gearbox at the operating point. This system can be solved using the modal transformation approach [18], where first the natural frequencies and eigenvectors of the vibration system are calculated. Then the vibration equation is transformed into modal coordinates by multiplication with the matrix of eigenvectors. Through the modal

transformation, instead of a *n*-degree-of-freedom system, *n*-decoupled single-mass oscillators result, whose vibration response can be calculated separately. By the final back transformation into the physical coordinates, delivers the sought solution to the oscillation problem.

Since the shafts and gears in the system under consideration are made of steel, it is a weakly damped system. According to Holzer [19], the damping coefficient must be about 175 times higher than the coefficient of steel for the damped natural frequencies to deviate by more than one percent from the natural frequencies of the undamped system. For this reason, the damping can initially be neglected. Formula 1 thus simplifies to:

$$M \cdot \ddot{x} + C_0 \cdot x = 0 \tag{4}$$

and leads to the general eigenvalue problem:

$$\left(C_0 - \omega^2 M\right) \cdot \varphi = 0. \tag{5}$$

The non-trivial results of this formula are *r* natural frequencies $\omega_i$ and the corresponding eigenvectors $\varphi_i$, which are combined into the eigenvector matrix $\Phi$ and can then be mass normalized:

$$\widetilde{\Phi} = \frac{-\Phi}{\sqrt{\Phi^T \cdot M \cdot \Phi}} \tag{6}$$

$\widetilde{\Phi}$   Normalized eigenvector matrix
$\Phi$   Eigenvector matrix
$M$   Mass matrix (kg)

The normalized eigenvector matrix is then used to normalize the system matrices, resulting in a unit matrix for the modal mass matrix $\widetilde{M}$

$$\widetilde{M} = \widetilde{\Phi}^T \cdot M \cdot \widetilde{\Phi} = \begin{pmatrix} 1 & & 0 \\ & \ddots & \\ 0 & & 1 \end{pmatrix}, \tag{7}$$

and a diagonal matrix with the eigenvalues $\omega_i^2$ as diagonal elements for the modal stiffness matrix $\widetilde{C}$:

$$\widetilde{C} = \widetilde{\Phi}^T \cdot C \cdot \widetilde{\Phi} = \begin{pmatrix} \omega_1^2 & & 0 \\ & \ddots & \\ 0 & & \omega_n^2 \end{pmatrix} \tag{8}$$

$n$   Number of degrees of freedom

With the system matrices and eigenvectors of the gearbox model, the global frequency response matrix *V* can be calculated, where $\Omega$ is the angular frequency of a harmonic load:

$$V(\Omega) = \Phi \cdot \left(-\Omega^2 \widetilde{M} + \widetilde{C}\right)^{-1} \cdot \Phi^T$$

$$= \begin{bmatrix} f_{11} & f_{12} & \cdots & f_{1n} \\ f_{21} & f_{22} & & \vdots \\ \vdots & & \ddots & \\ f_{n1} & \cdots & & f_{nn} \end{bmatrix} \tag{9}$$

$V$   Frequency response matrix (m/N; rad/Nmm)
$f_{nn}$   Transfer functions from DOF *n* to *n* (m/N; rad/Nmm)

The frequency response matrix allows the calculation of the undamped system response to a harmonic force excitation for each node and degree of freedom in the model, which is used to analyse the high-speed-planetary gearbox in Chap. 8.

The amplitudes of the deflections $\check{u}$ in the system can subsequently be calculated with the frequency response matrix and the amplitudes of harmonic excitations $\check{f}$ to:
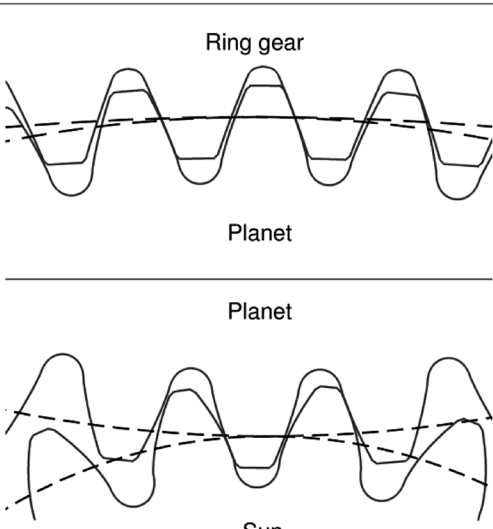
$$\check{u}(\Omega) = \Phi \cdot \left(-\Omega^2 \widetilde{M} + \widetilde{C}\right)^{-1} \cdot \Phi^T \cdot \check{f}(\Omega)$$
$$= V(\Omega) \cdot \check{f}(\Omega) \tag{10}$$

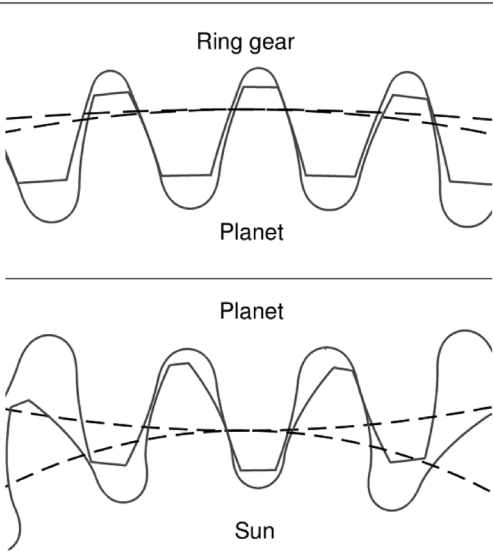## 2 Gear macro geometries of the Speed4E-gearbox in ST1

Stage 1 in ST1 represents a high-ratio planetary stage in the configuration as an orbiting planetary gear. To investigate relevant influencing parameters on the excitation behavior of the planetary stage, two different gear geometries were manufactured and tested. The reference variant represents a balanced design with respect to efficiency and excitation behavior. In addition, an NVH-optimized gearing variant with high overlap ratios is being investigated, in which an enhanced vibration behavior is expected.

The gear geometries in the transverse section and relevant parameters of the gear variants are listed in Fig. 3 and 4. Both variants have a center distance of a = 48.5 mm as well as a common gear width of b = 18.75 mm and can thus be exchanged, experimentally investigated, and compared without further adjustments in the gearbox housing. Both gearing variants have overlap ratios slightly above the integer values of one and two to ensure a generally low excitation level. Due to the low torques of the high-speed EM, the gears in stage 1 generally have comparatively low

**Fig. 3** Transverse section and gear parameters of reference variant

| Transverse section | | Descr. | Unit | Sun | Planet | Ring |
|---|---|---|---|---|---|---|
| Ring gear<br>Planet<br>Planet<br>Sun | | $m_n$ | mm | | 1.09 | |
| | | $\alpha_n$ | ° | | 20 | |
| | | $\beta$ | ° | | 11.5 | |
| | | $z$ | - | 24 | 63 | -150 |
| | | $x^*$ | - | 0.24 | -0.03 | -0.17 |
| | | $d_{Na}$ | mm | 29.3 | 71.7 | -165.3 |
| | | $d_f$ | mm | 24.08 | 66.81 | -169.9 |
| | | $b$ | mm | 19.75 | 18.75 | 19.75 |
| | | $a$ | mm | 48.5 | | |
| | | | | -48.5 | | |
| | | $\epsilon_{\gamma,\alpha,\beta}$ | - | 2.55/1.46/1.09 | | |
| | | | | 2.54/1.45/1.09 | | |
| | | $H_v$ | - | 0.131 | | |
| | | | | 0.022 | | |

**Fig. 4** Transverse section and gear parameters of NVH-optimized variant

| Transverse section | | Descr. | Unit | Sun | Planet | Ring |
|---|---|---|---|---|---|---|
| Ring gear<br>Planet<br>Planet<br>Sun | | $m_n$ | mm | | 1.12 | |
| | | $\alpha_n$ | ° | | 17.5 | |
| | | $\beta$ | ° | | 23.3 | |
| | | $z$ | - | 23 | 57 | -136 |
| | | $x^*$ | - | 0.2 | -0.6 | 0.47 |
| | | $d_{Na}$ | mm | 29.3 | 71.7 | -165.3 |
| | | $d_f$ | mm | 24.08 | 66.81 | -169.9 |
| | | $b$ | mm | 19.75 | 18.75 | 19.75 |
| | | $a$ | mm | 48.5 | | |
| | | | | -48.5 | | |
| | | $\epsilon_{\gamma,\alpha,\beta}$ | - | 4.14/2.04/2.10 | | |
| | | | | 4.11/2.01/2.10 | | |
| | | $H_v$ | - | 0.215 | | |
| | | | | 0.045 | | |

normal moduli in the range of approx. one millimeter. The NVH variant has slightly larger teeth and has a normal module of $m_n = 1.12$ mm, while the normal module for the reference variant is $m_n = 1.09$ mm.

The lower tooth height in conjunction with the higher operating pressure angle $\alpha_n$ leads to smaller contact ratios $\varepsilon_\alpha$ for the reference variant, which results in a smaller and thus better tooth loss factor $H_V$, but also means that less favorable vibration behavior can be expected. Due to the number of teeth, the meshing sequence is symmetrical for the reference variant and sequential for the NVH-optimized variant.

## 3 Application of the frequency response procedure for efficient quasi-dynamic simulation of the vibration behavior

The mass and stiffness matrices of the gearbox are calculated with the RIKOR simulation program developed at FZG. RIKOR is a software for calculating the elastic load and deformation behavior of transmission systems. The program is essentially based on analytical approaches to model a real continuous system through discrete rigid bodies or nodes who are connected through stiffnesses and have masses in accordance to the modelling of the shafts. A de-
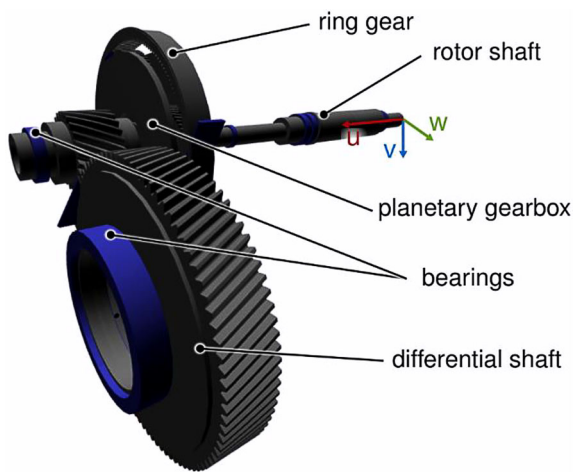
**Fig. 5** Modelling of the elastic system ST1 in RIKOR

tailed description of the modeling process in RIKOR can be found in [20]. In contrast to Bihr [17], who used a reduced model, the entire transmission system is used for the modeling, which means that all degrees of freedom and excitations also in case of multi-stage transmission systems are included. Figure 5 visualizes the elastic gearbox model of ST1 in RIKOR including the rotor and differential shafts and coordinate system. The u-axis points in the axial direction coaxial to the sun, v- and w-direction are correspondingly the radial coordinate directions. The tooth meshing is mapped by fully coupled spring elements according to Weber-Banaschek [21], depending on the meshing position. All shafts including the planet carrier and ring gear are modelled analytically as elastic Timoshenko [22] beam elements. Also marked in the figure is the calculation node 174 in the system, which represents the axial center of the

ring gear and is closest to the position of sensor Ch1. As all nodes in the system have six degrees of freedom (DOF) (three translational, three rotational), the translational degrees of freedom in the system of node 174 are DOF 1041-1039.

The diagram in Fig. 6 is the undamped translational transfer functions at the ring gear for 1000 discrete harmonic excitation frequencies from 0–20 kHz on a logarithmic scale. The curve thus represents the undamped vibration response of the ring gear due to a harmonic force excitation versus the frequency. In axial u-direction, the highest peak occurs at approx. 10.4 kHz and in the radial directions approx. 12.5 kHz. There are also peaks with lower amplitudes at approx. 4 kHz. These transfer functions can now be offset against the excitations on the ring gear to calculate the harmonic vibration response.

Figure 7 shows the time-varying forces $\mathbf{f_d}(t)$ calculated in RIKOR at the ring gear in the three translational directions over 20° revolution in the time domain on the left and an input torque of 20 Nm. The amplitudes of the forces acting on the ring gear in the axial direction (u) are higher than the values for the radial directions. This behavior is according to expectation, since the radial forces between planets and ring gear partially cancel out each other while the axial forces add up over the meshes due to the symmetric meshing sequence. The diagram on the right shows the spectrum of the force curve on the ring gear in the three directions. The highest amplitudes of around 19 N for the u-direction are reached for the 1st tooth meshing order (TMO), which occurs at the 150th shaft order of the planet carrier (CO). Lower amplitudes can also be seen at the higher harmonic TMO and at low order due to the excitation by the second stage of ST1. The radial excitations

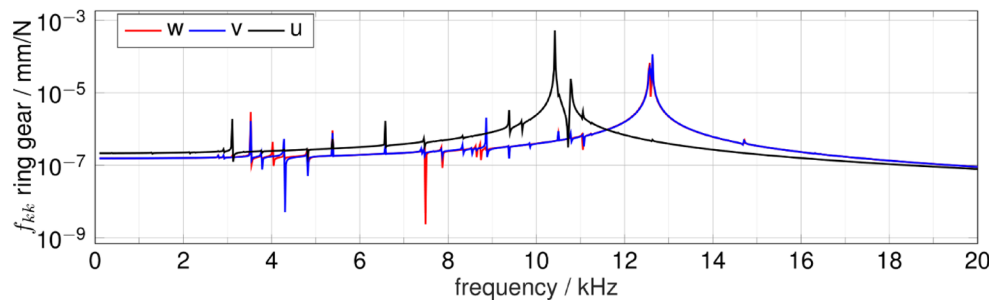**Fig. 6** Translational transfer functions at the ring gear
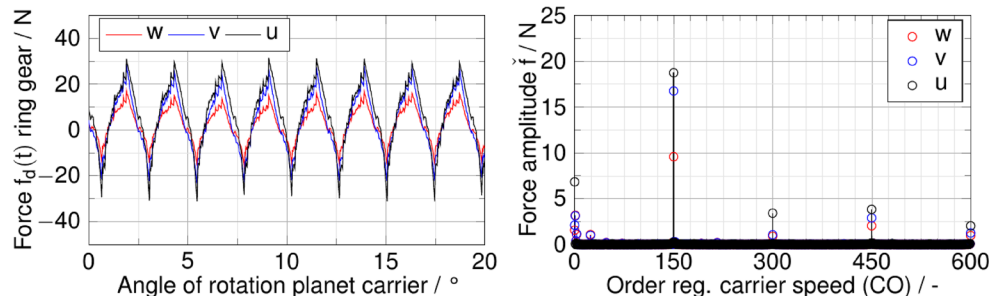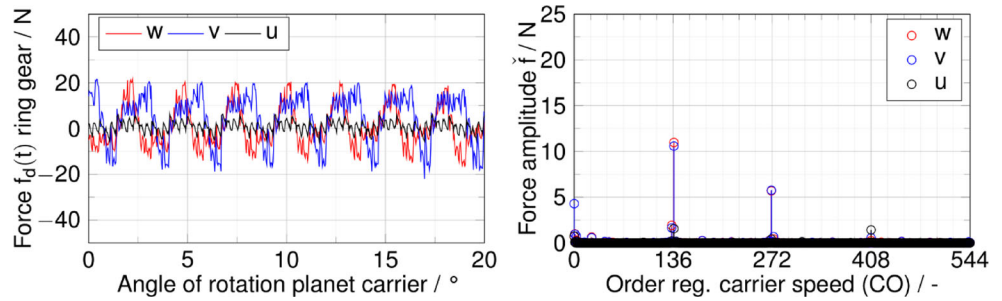


**Fig. 7** Reference variant. (Force curve (left) and spectrum of the force curves on the ring gear (node 174) and an input torque of 20 Nm)

**Fig. 8** NVH-opt. variant. (Force curve (left) and spectrum of the force curves on the ring gear (node 174) and an input torque of 20 Nm)



**Fig. 9** Frequency diagrams of virtual speed ramp-ups at 20 Nm input torque for the reference (left) and NVH-optimized variant (right)
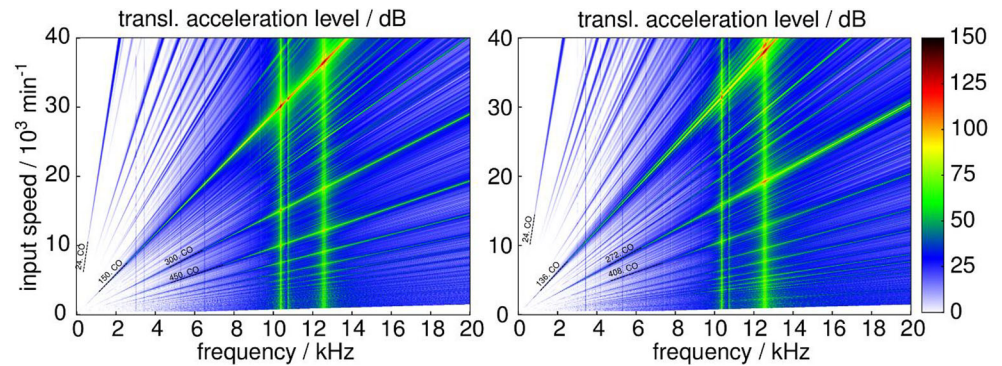


are the results of the elasticities in the model, which lead to an eccentric displacement of the planet carrier and, thus, an uneven load sharing between the planets. This uneven load sharing causes the meshing to lose symmetry and thus leads to resulting radial excitations.

The results of the calculation for the NVH-optimized variant can be seen in Fig. 8. Due to the sequential meshing sequence, the axial force fluctuation is much lower as the fluctuation in radial direction and reaches only around 2 N at the 1st tooth meshing order (TMO). Although the NVH-optimized variant has a much lower excitation level, the sequential meshing sequence nevertheless results in force amplitudes in the radial directions that are comparable to the reference variant.

By scaling the order spectrums $\check{f}$ shown in Figs. 7 and 8 with the speed and multiplying it with the transfer function according to formula (10), a spectrum of the displacements is obtained for each speed step and frequency. With the amplitudes and frequencies for each speed step, the corresponding acceleration spectrum can be calculated. Figure 9 shows the undamped translational acceleration levels for the reference and NVH-optimized variant in frequency diagrams, calculated according to the presented frequency response method. The calculated vibration behavior at the ring gear is determined by a resonance phenomenon at ap-

**Table 1** Max. calculated acceleration levels for Reference- and NVH-optimized variant

| | Max. acceleration level/dB |
|---|---|
| Reference | 152.4 |
| NVH-optimized | 138.5 |

prox. 10.4 kHz, which matches the peak of the transfer functions. The 1st tooth meshing order (TMO) in the reference variant occurs at the 150th shaft order of the planet carrier (CO) and is visible as origin straight line and meets the natural frequency of the planetary gear at around 30,000 rpm, resulting in significant level peaks in this speed range. Further peaks occur at the corresponding pre-resonances of the higher harmonics of the TMO with the resonant frequency. Lower acceleration levels occur at 12.5 kHz, where radial excitations meet resonances in radial direction.

For the NVH-optimized variant, the resonances in axial direction are less pronounced, as the axial excitations are lower in this direction. The acceleration levels in radial direction at 12.5 kHz are almost the same, as the excitation has similar amplitudes. Table 1 shows the calculated max., undamped acceleration levels of the reference and NVH-optimized variant. The max. acceleration of the NVH-optimized variant is 13.9 dB lower as for the reference variant, due to the lower axial excitation coming from the meshing.

## 4 Test rig setup for experimental investigation of the high-speed powertrain

Figure 10 visualizes the test rig setup at the Gear Research Center (FZG) from the technical university of Munich (TUM). The heart of the test facility is the Speed4E powertrain with the drive machines EM1 and EM2 and the high-speed test gearbox. In traction mode, the power electronic is supplied by an 800 V DC voltage source. The

power at the gearbox output is absorbed by two identical load machines, operating in generator mode. The electrical power generated by the load machines is fed back into the electrical grid via a regenerative power supply unit. The test rig is furthermore equipped with a large number of sensors for comprehensive investigations of the efficiency and vibration behavior of the high-speed gearbox. The reaction torque measurement concept of pendulum machines [23] is used to measure the input torque. The output torque is measured via torque-measuring shafts. The investigations of the vibration behavior of the gearbox are carried out by acceleration sensors.that are mounted on the gearbox housing.

Figure 11 shows the positions of the sensors to evaluate the vibration behavior of ST1. Since this study focuses on the excitation behavior of the high-speed planetary gearbox, the results of sensor ch1 are primarily used for analysis below. Sensor ch1 is positioned directly above the ring gear on the housing surface. The sensors that are used are uniaxial accelerometers of the type Brüel&Kjaer 4518, which operate according to the piezoelectric principle. They have a sensitivity of 10 mV/g, and are generally characterized by a sensor response of high quality. The high natural frequency of the sensors of approx. 45 kHz enables the detection of a wide spectrum from 1 to 20 kHz, which covers the audible frequency range and is thus also suitable for the evaluation of the gear excitation for the application case of the high-speed gearbox.

## 4.1 Test program and test evaluation

The acceleration measurements on the gearbox housing take place during linear and continuous speed ramp-ups with constant drive torque. Figure 12 shows the speed and torque curve of an exemplary run-up measurement at 20 Nm drive torque. The speed ramp-ups are started at a sun speed of 400 rpm, at which the torque was previously applied. The test procedure shown is carried out in this way for the reference and NVH-optimized variant. Before the acceleration measurements, the gears run through a run-in program lasting several hours to smooth the surface roughness of the gear flanks and rolling bearings mounted in the new condition. Oil is supplied by injection lubrication with a dry sump at an oil injection temperature of 40 °C. The evaluation of the measured acceleration signals is performed with a program based on the Kennwerthauptprogramm (engl. Characteristic-value-main-program) [24] of FZG. The basis of the evaluation is first a fast Fourier transformation (FFT) with a Hanning window [25, 26] for the transfer of the raw data from time to spectral space. If necessary, resampling



**Fig. 10** Speed4E test rig setup for vibration measurements
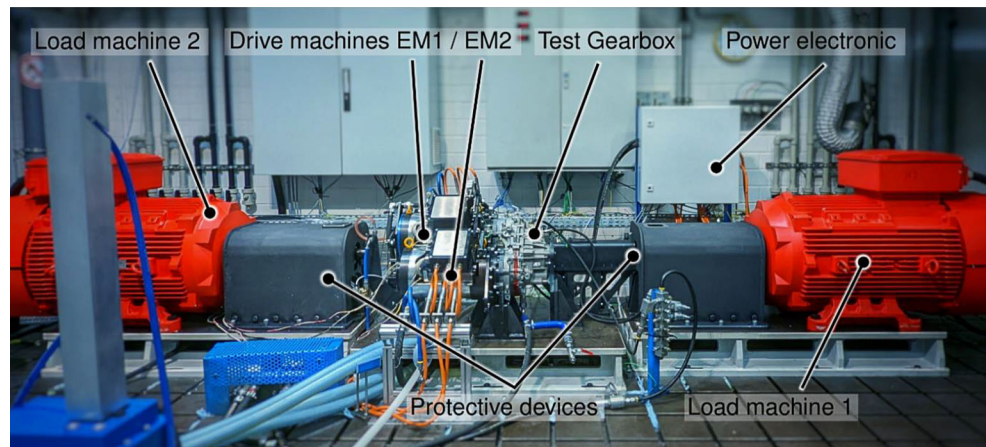


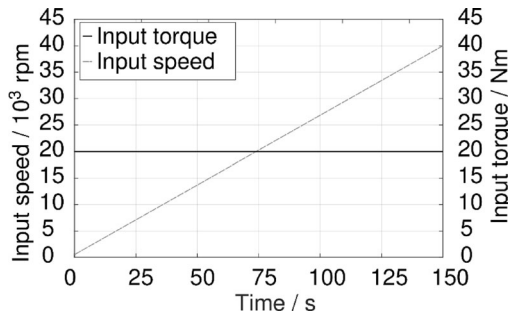**Fig. 11** Sensor positions for vibration measurements of high-speed gearbox ST1
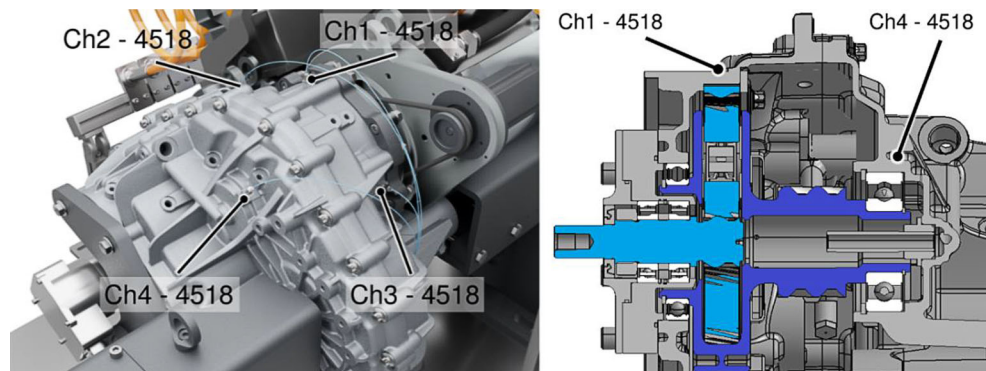
**Fig. 12** Exemplary curve of the speed and torque of a test run at 20 Nm input torque

or zero-padding is used to adjust the block length in the FFT. The frequency components are then leveled according to

$$L_k = 20 \cdot dB \cdot \log_{10}\left(\frac{x_w \cdot 10^{-3}}{x_0}\right). \tag{11}$$

$L_k$     Structure-borne sound level (dB)
$x_w$     Amplitude of measured acceleration (m/s²)
$x_0$     Ref. val.: $x_0 = 10^{-6}$ m/s² (m/s²)

All evaluations are performed with 1000 discrete speed steps at an order resolution of 0.3 and a frequency resolution of 15 Hz in the frequency range of 0–20 kHz. To characterize the vibration behavior of the high-speed gearbox, the following evaluation and display methods are used in particular:

### 4.2 Campbell diagram in frequency representation

The spectra of the acceleration measurements created with the methods described above are determined for each speed step or defined time window and displayed in the form of Campbell diagrams above the speed. This evaluation method allows the identification of critical speed or frequency ranges.

### 4.3 Averaged frequency and order spectrum

For a holistic evaluation of the determining excitation sources in the system, an averaging of the individual spectra calculated for the Campbell diagrams can be performed. For this purpose, the unlevelled amplitudes of the spectra of each speed step are averaged and then the levelling is performed. In the case of speed ramps, the result of the averaging is then an averaged spectrum over the speed in frequency or order representation.

### 4.4 Level curves of arbitrary excitation orders versus rotational speed

The determined individual spectra of all speed stages can also be used to isolate amplitudes or level curves of any excitation orders such as tooth meshing orders, rotor orders, or any other shaft orders to display them above the speed. This allows the determination of excitation sources to be identified and displayed side by side over the speed.

## 5 Results of the vibration measurements for the reference variant in ST1

This section deals with the experimental results regarding the vibration behavior of the high-speed planetary gear in the reference variant over the entire speed and frequency range. In particular, resonance phenomena and gear excitation are discussed.

Figure 13 shows the frequency diagram of the speed ramp-up at 20 Nm drive torque. Visible are the 1st, 2nd, and 3rd TMO, which occur at the 150th, 300th, and 450th (CO) with distinct sidebands. The structure-borne sound measurement is determined by the resonance between the 1st TMO and the natural frequency of the planetary gearbox (PG), at around the frequency of about 10.5 kHz, which was already predicted by the previous calculation results. The calculation also showed resonance peaks in radial direction at around 12.5 kHz. The reason why these resonances are not so clearly visible in the measurement could be that the ring gear is fixed with radial clearance and therefore reacts very flexible in radial direction in reality.

Also noticeable are peaks with large excitation levels in the speed range above 30,000 rpm and in the low-frequency range ($\approx$ 0–2 kHz), which can be assigned in particular to the 7.25th and 21.75th CO. Due to the gear ratio of the reference variant of $i_{ref} = 7.25$, these CO corresponds to the 1st
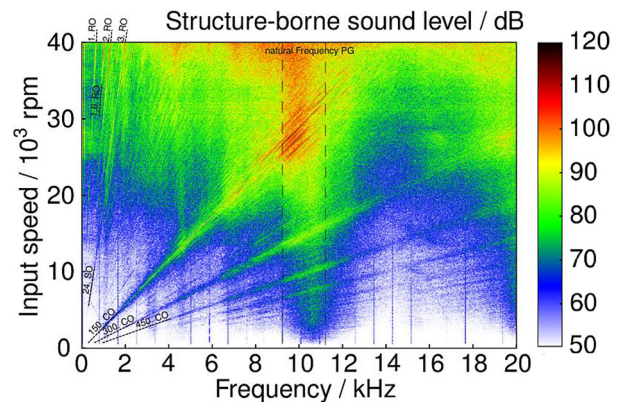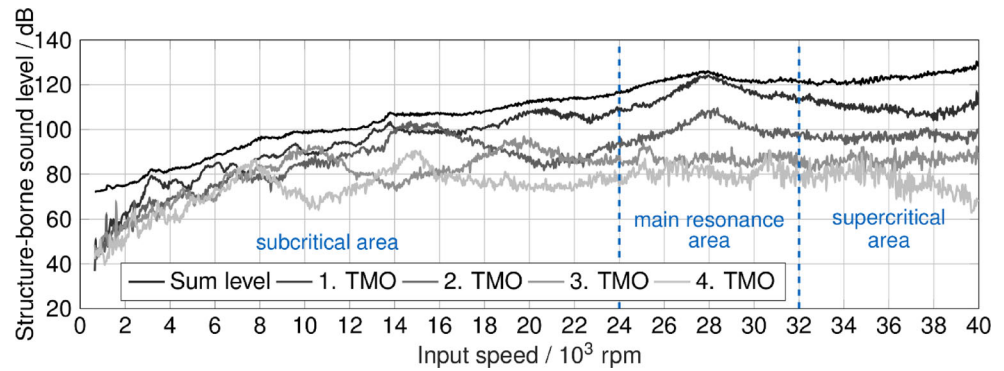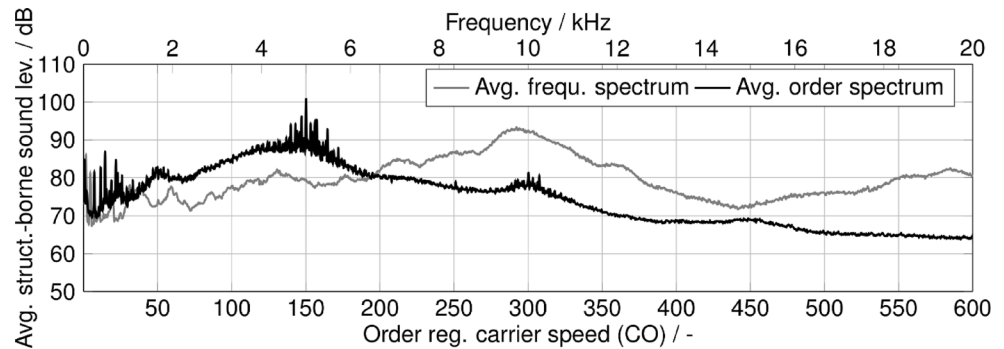


**Fig. 13** Reference variant. (Frequency diagram of a speed ramp-up with input torque 20 Nm)
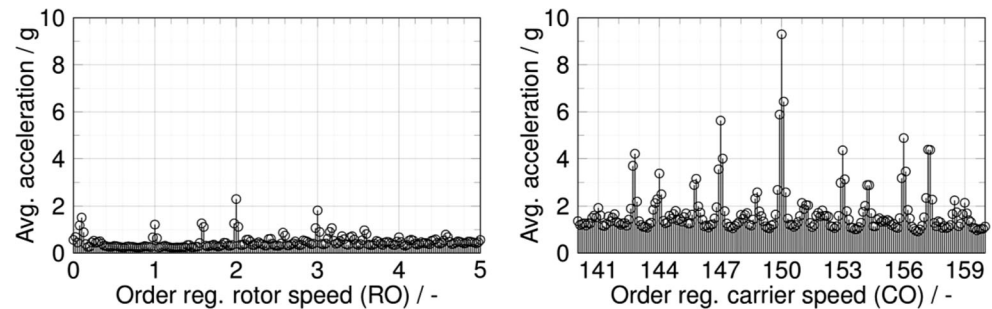
**Fig. 14** Reference variant. (Curves of the sum level and the 1st–4th TMO of a speed run-up at an input torque of 20 Nm)



**Fig. 15** Reference variant. (Averaged frequency and order spectrum of a speed ramp-up at an input torque of 20 Nm)



**Fig. 16** Reference variant. (Averaged order spectrum of low rotor orders (left) and orders around the TMO (150th CO))



and 3rd orders of the rotor shaft (RO). Causes of the low-frequency excitations include, in particular, effects from the rotor dynamics due to imbalances of the rotor and gearbox input shafts or other dimensional deviations such as axial or angular misalignments between the driving shafts separated by the shaft coupling. Unbalance due to electromagnetic influences can be a result of non-symmetrical voltage characteristics in the windings at high speeds can also not be excluded as a cause. In the high-speed range, the acceleration level of the 1.6th RO rises sharply, which can be assigned to the rollover frequency of the rolling elements on the outer ring or the planet bearings. This phenomenon points strongly to increasing bearing loads due to the centrifugal forces in the PG.

The curves of the 1st–4th TMO and the sum levels over all frequencies and the rotational speed can be seen in Fig. 14. The level curve of the 1st TMO illustrates once again the determining character of the resonance range already described. The measured acceleration level there rises to 124 dB and thus contributes significantly to the sum level. The higher harmonic TMOs come into resonance in each case in the range of half the speed and becomes the determining excitation source of the gear teeth there.

Figure 15 shows the averaged frequency and order spectrum of the speed ramp-up. The natural frequency of the PG leads to a clear maximum in the frequency spectrum at about 10 kHz. In the averaged order spectrum, the maximum is at the 150th CO. The higher harmonic TMO are equally visible but show much lower acceleration levels. The rotor dynamic excitations mentioned before are visible in the form of peaks at lower CO ($< 50$ CO).

Figure 16 on the left illustrates the averaged linear accelerations of the low RO of the speed run-up. The 2nd rotor order shows the highest acceleration values with a good 2 g on average. In addition, the 1st and 3rd RO as well as the excitation order are visible, which belong to the rollover
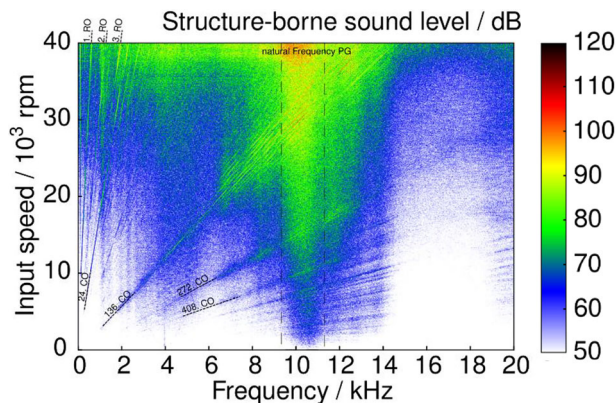
**Fig. 17** NVH-opt. variant. (Curves of the sum level and the 1st–4th TMO of a speed run-up at an input torque of 20 Nm)
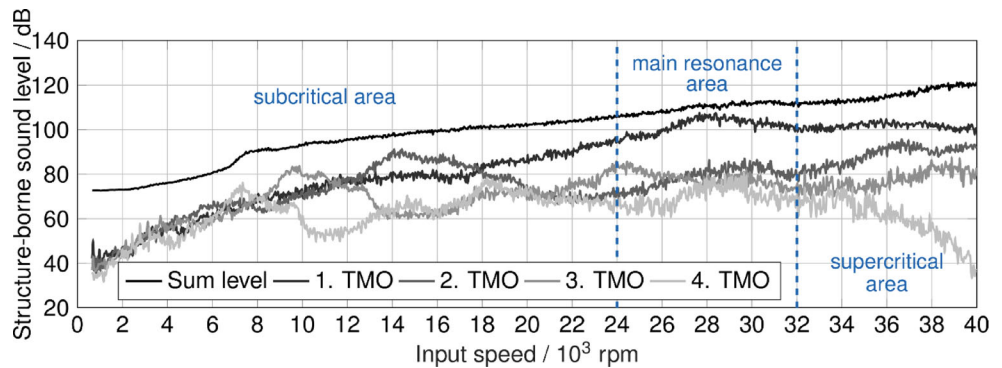


frequency of the rolling elements on the outer ring of the planetary bearings. The averaged accelerations in the region of the 1st TMO show significantly higher values of a good 9 g. Due to the symmetrical meshing sequence, the highest acceleration values in the case of the reference variant occur exactly at the 1st TMO and the 150th CO, respectively. High accelerations also show the frequencies with a distance of ±3 and ±6 CO to the 1st TMO at the 147th, 144th, 153rd, and 156th CO, which typically result from amplitude and frequency modulation due to manufacturing assembly, deformation-related deviations or further deviations in the system. In the supercritical range, the excitation level of the gearing decreases significantly again and the rotor dynamic excitations become more important.

## 6 Results of the vibration measurements for the NVH-optimized variant in ST1

Figure 18 shows the frequency diagram of the speed ramp-up at a constant input torque of 20 Nm at sensor Ch1 for the NVH-optimized variant. The vibration behavior is again primarily determined by the natural frequency of the planetary gearbox and the corresponding resonant and pre-resonant areas. The 1st TMO (136th CO) and the higher harmonics are also visible but show significantly lower acceler-

ation levels in comparison to the reference variant. The 1st TMO of stage 2 (24th CO) is more evident since the general excitation level by stage 1 is lower. In the high-speed range, low RO (1st, 2nd, 3rd) again develop significantly increasing acceleration levels, analogous to the reference variant. The curves of the 1st–4th TMO in Fig. 17 clarify the significantly better excitation behavior of the NVH-optimized variant. The acceleration levels of the 1st TMO are significantly below the values for the reference variant. The maximum value in the main resonance range rises to just 107 dB and is thus about 17 dB lower than the reference variant. Overall, the acceleration levels of the NVH variant are significantly below the sum level over the entire speed range, suggesting a lower contribution of the gears to the overall vibration behavior characteristics.

The averaged order spectra of the run-ups of the NVH-optimized and reference variant in comparison are shown in Fig. 19. Again, pronounced sidebands are visible around the 1st TMO (136th CO), although the 136th CO is suppressed due to the sequential meshing sequence in the case of the NVH-optimized variant, and, in particular, sidebands with a spacing of whole multiples of CO appear. The averaged acceleration level for the area around the 1st TMO only reaches values of just below 90 dB for the NVH-optimized variant, which represents a significant difference of a good 10 dB compared to the reference variant ($\approx$ 100 dB). The averaged frequency spectrum clearly shows the natural frequency of the planetary gearbox, which also occurs for the NVH variant around 10 kHz.

Figure 20 illustrates the averaged linear accelerations of the low RO of the speed run-up on the left and the order spectrum around the TMO (136th CO) for the NVH-optimized variant (right). Due to the sequential meshing sequence, the maximum amplitude does not appear at the TMO (136th CO), but in the distance of integer CO's, whereby the maximum occurs at the 138th TMO. At a good 2 g, the averaged amplitudes around the TMO are well below the averaged values of the reference variant (a good 9 g). The lower rotor orders also show significantly lower average amplitudes, which can be attributed to the generally



**Fig. 18** NVH-opt. variant. (Frequency diagram of a speed ramp-up with input torque 20 Nm)

**Fig. 19** Averaged order spectra of the NVH-optimized and reference variant of a speed ramp-up at an input torque of 20 Nm
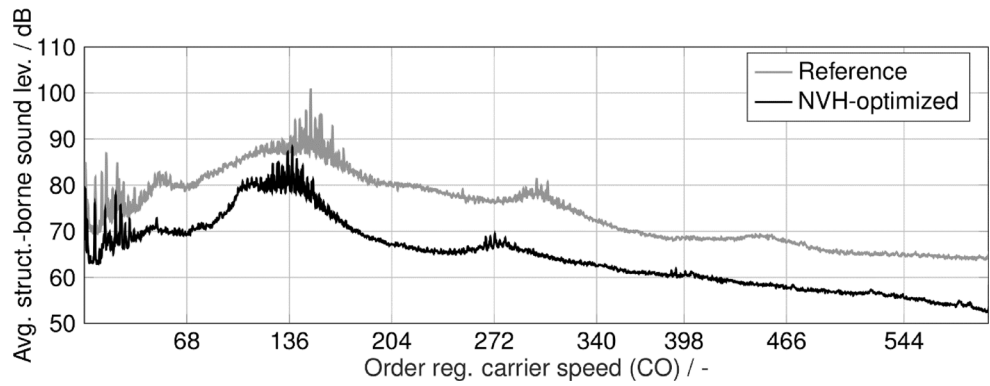


**Fig. 20** NVH-opt. variant. (Averaged order spectrum of low rotor orders (left) and orders around the TMO (136th CO))
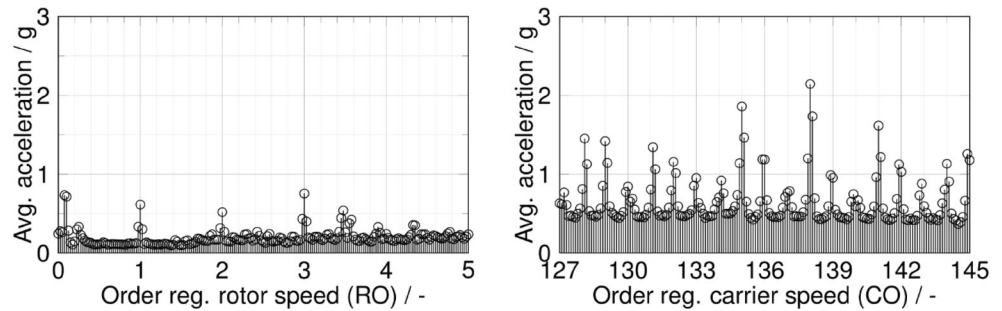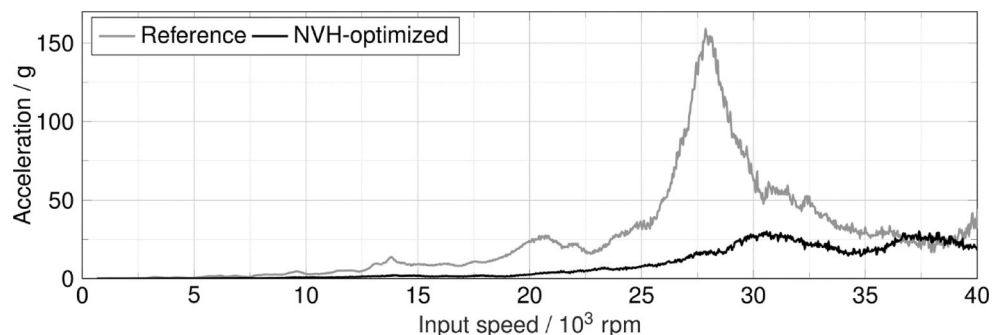


lower level of acceleration in the entire frequency range for the NVH-optimized variant.

## 7 Resonance curves of the gearing variants

Figure 21 illustrates the resonance curves of the reference and NVH-optimized variant as acceleration values of the 1st TMO over the input speed at an input torque of 20 Nm. In the case of the reference gearing, the accelerations already increase significantly in the subcritical operating range at 14,000 rpm and a good 20,000 rpm, before accelerations of up to over 150 g are then reached in the main resonance area.

## 8 Summary and outlook

In this article, the vibration behavior of the high-speed planetary gearbox of the high-speed electromechanical powertrain from the Speed4E research project is analyzed numerically and experimentally for two different gear geometries. The numerical investigations were carried out using a frequency response method presented, which, based on the analytical gear calculation program RIKOR, represents a highly efficient method for a quasi-dynamic simulation of the vibration behavior of gearboxes. Especially compared to full FE-based MBS programs, the method represents a computationally efficient procedure.

The experimental investigations fundamentally confirm the numerical results, since the resonance phenomenon of the planetary gear at approx. 10 kHz, which is pronounced

**Fig. 21** Resonance curve of Reference and NVH-optimized variant as acceleration of 1st TMO and sorounding at an input torque of 20 Nm

in the calculation, also determines the vibration behavior in the experiment.

In the supercritical speed range (>32,000 rpm), excitation orders of lower frequencies are shown to be dominant, which is most likely to be attributed to imbalances and other deviations of the fast-rotating driving shafts.

The NVH-optimized gearing variant shows significantly better vibration behavior compared to the reference variant. The results suggest that high overall contact ratios of the gears are necessary for the application in high-speed transmissions to achieve acceptable NVH behavior.

In further investigations, it is planned to analyze the vibration behavior of the high-speed transmission in other load ranges as well as over the entire characteristic map of the electric machine, in order to be able to describe load-dependent phenomena as well.

The presented frequency response method is also applied and extended for the NVH variant in order to be able to perform deviation-related analyses with imaging of sidebands.

# References

1. Schweigert D, Mileti M, Morhard B, Sedlmair M, Fromberger M, Otto M, Lohner T, Stahl K (2019) Innovative transmission concept for hyper-high speed electro-mechanical powertrains. Dritev – Drivetrain for. Vehicles
2. Morhard B, Schweigert D, Mileti M, Sedlmair M, Lohner T, Stahl K (2021) Efficient lubrication of a high-speed electromechanical powertrain with holistic thermal management. Forsch Ingenieurwes 85:
3. Schweigert D, Morhard B, Otto M, Stahl K (2022) Results of the joint project Speed4E, efficiency and vibration behavior of the high-speed gearbox. E-Motive. Expert, Forum Vehicle Drives
4. Merwerth J (2014) The Hybrid-Synchronous Machine of the New BMW i3&i8: Challenges with Electric Traction Drives for. Veh workshop Univ Lund
5. Schweigert D, Gerlach M, Hoffmann A, Morhard B, Tripps A, Lohner T, Otto M, Ponick B, Stahl K (2020) On the Impact of Maximum Speed on the Power Density of Electromechanical Powertrains. Vehicles 2:365–397. https://doi.org/10.3390/vehicles2020020
6. Deiml M, Eriksson T, Schneck M, Tan-Kim A (2019) Hochdrehende E-Antriebseinheit für die nächste Fahrzeuggeneration. ATZ. Automob Z 121:42–47. https://doi.org/10.1007/s35148-019-0045-8
7. Zeller P (2018) Handbuch Fahrzeugakustik, 3rd edn. Springer, Wiesbaden. ISBN 978-3-8348-0651-2.
8. Ulz A, Graf B, Priestner C, Mehrgou M (2021) Kriterien für die NVH-Entwicklung von elektrischen. Antriebseinheiten atz – Automob Z 123:26–33. https://doi.org/10.1007/s35148-021-0713-3
9. Wang S, Jouvray J, Kalos T (2018) NVH Technologies and Challenges on Electric Powertrain. Sae Tech Pap 1551:2018–2001
10. Chavan C, Heidlauf T, Langhart J (2020) Gearbox simulation for EVs: Optimization between gear rating, available space and NVH requirements. 20. Internationales Stuttgarter. Symposium. https://doi.org/10.1007/978-3-658-29943-9_24
11. Feng S, Qu R (2022) NVH Analysis of Integrated Motor and Two-Speed Gearbox System for Electric Vehicles. International Conference on. Electric, al Machines (ICEM), pp 115–121 https://doi.org/10.1109/ICEM51905.2022.9910838
12. Xianghuan L (2018) High-speed BEV Reducer NVH Performance Optimization and Experimentation. Eng Appl Sci 3:103. https://doi.org/10.11648/j.eas.20180304.12
13. Zhang Y, Du J, Mao J, Xu M (2020) Dynamic Analysis of High-Speed Helical Gear Transmission in Pure Electric Vehicle Gearbox. Shock and. Vibration, vol 2020, pp 1–19 https://doi.org/10.1155/2020/6639372
14. Mbarek A, Hammami A, Fernandez Del Rincon A, Chaari F, Viadero Rueda F, Haddar M (2019) Effect of load and meshing stiffness variation on modal properties of planetary gear. Appl Acoust 147:32–43. https://doi.org/10.1016/j.apacoust.2017.08.010
15. Inalpolat M, Kahraman A (2009) A theoretical and experimental investigation of modulation sidebands of planetary gear sets. J Sound Vib 323:677–696. https://doi.org/10.1016/j.jsv.2009.01.004
16. Kücükay F (1987) Dynamik der Zahnradgetriebe: Modelle, Verfahren, Verhalten; Springer Berlin Heidelberg ISBN 978-3-540-17111-9.
17. Bihr J (2016) Untersuchung des Schwingungsverhaltens von mehrstufigen Stirnradgetrieben unter besonderer Berücksichtigung des Welle-Lager-Systems. Dissertation, Technische Universität München
18. Gasch R, Knothe K (1987) Kontinua und ihre Diskretisierung. Strukturdynamik, vol 1. Springer Berlin Heidelberg. ISBN 978-3-540-17111-9.
19. Holzer H (1921) Die Berechnung der Drehschwingungen und ihre Anwendung im Maschinenbau. Springer Berlin Heidelberg. ISBN 978-3-642-51268-1.
20. Weinberger U, Otto MK, Stahl K (2019) Closed-Form Calculation of Lead Flank Modification Proposal for Spur and Helical Gear Stages. J Mech Des. https://doi.org/10.1115/1.4045396
21. Weber C, Banaschek K (1955) Schriftenreihe Antriebstechnik. Formänderung und Profilrücknahme bei gerad- und schrägverzahnten Rädern, vol 11. Braunschweig

22. Timoshenko S, Goodier JN (1970) Theory of Elasticity, Third. Mc-Graw-Hill, New York

23. Pointner L, Pflaum H, Stahl K (2021) Test Facility to Investigate Function and Efficiency of the Speed4E Hyper-High-Speed Electromechanical Powertrain. STLE Annual Meeting & Exhibition

24. Utakapan T, Ingeli J, Heider M, Otto M, Stahl K (2014) IV – Heft 1101 – Neue Kennwerte zur rechnerischen Beurteilung des Anregungsverhaltens von Verzahnungen. Abschlussbericht; Forschungsvereinigung Antriebstechnik e.V. Nr, vol 487. FVA, Frankfurt/Main

25. Harris FJ (1978) On the use of windows for harmonic analysis with the discrete Fourier transform. Proc Ieee 66:51–83. https://doi.org/10.1109/PROC.1978.10837

26. Blackman RB, Tukey JW (1958) The measurement of power spectra from the point of view of communications engineering—Part I. Bell Syst Tech J 37:185–282. https://doi.org/10.1002/j.1538-7305.1958.tb03874.x